This article has been accepted for publication in IEEE Transactions on Transportation Electrification. This is the author's version which has not been fully edited and content may change prior to final publication. Citation information: DOI 10.1109/TTE.2023.3236526

Piecewise Affine Maximum Torque per Ampere for the Wound Rotor Synchronous Machine

Bernard Steyaert, *Student Member, IEEE*, Ethan Swint, *Member, IEEE*, W. Wesley Pennington, *Member, IEEE*, Matthias Preindl, *Senior Member, IEEE*,

***Abstract*—Power-efficient torque control of the Wound Rotor Synchronous Machine (WRSM) below base speed requires a minimization of electrical losses, namely copper losses. In this paper, the Maximum Torque per Ampere (MTPA) optimization problem is presented and solved using a convex pareto frontier of simulated or measured data points. Three filtered solution sets are mapped to current space using piecewise affine functions, which approximate the current using a piecewise linear function for a given torque. This set of piecewise linear functions enables a machine controller to implement MTPA online or as an offline lookup table. Simulated and experimental results are presented for a 65 kW, FEA-sampled WRSM. Compared to linear MTPA, the PWA MTPA functions are shown to reduce torque error by $> 25\%$, reduce average copper loss by $> 20\%$.**

***Index Terms*—Loss Minimization, Motor Parameters, Piecewise Linear Techniques, Torque Control, Wound Rotor Synchronous Machine**

This research is the continuation of the paper "Piecewise Affine Maximum Torque per Ampere for the Wound Rotor Synchronous Machine" presented at the 2022 IEEE Transportation Electrification Conference and AIAA/IEEE Electric Aircraft Technologies Symposium [1].

I. Introduction

The focus of this research is to minimize copper losses of the wound rotor synchronous machine (WRSM) given a desired torque. WRSMs are a class of electric machines used in industrial and residential applications including transportation (e.g., electric vehicles, EVs), power generation, and more.

Although recently WRSMs have shown their effectiveness in the EV space (the Renault Zoe vehicle uses WRSMs since 2012 [2]), WRSMs have been used primarily in power generation (10 MVA - 2200 MVA) for decades [3], [4]. WRSMs have numerous advantages over their permanent magnet synchronous machine (PMSM) counterpart, including: a higher base speed, reduced cost given that no expensive, rare-earth magnets are included in assembly, and their ability to modulate rotor flux leads to higher level of controllability. One advantage of this is the reduction of the volt-amp (VA) rating of the inverter by direct power factor correction [5]. Another advantage is that at high torque, low speed operation (common in EVs) this modulation can be used to decrease the stator current, reducing cost [3]. However, there are disadvantages to using WRSMs as opposed to PMSMs such as: increased mechanical complexity, lower power density, and higher copper losses due to the added rotor windings. Finally, a strong, nonlinear coupling between the direct (d) and rotor (r) dimensions exists in WRSMs.

Machine controllers are able to directly control and regulate some combination of voltage, current, or flux. This makes controlling torque generally difficult. The most common approach is to define a set of reference currents for any given reference torque. Because torque is a non-convex function of current [6], the mapping is generally not unique, and there is no optimal solution to minimize copper losses. In literature, solutions to this problem are referred to as Maximum Torque per Ampere (MTPA). To prevent high flux error during saturation and cross-saturation, the WRSM must operate in the linear and non-linear regions of the magnetic model [7]–[15]. This makes the MTPA problem for the WRSM more complicated than for the PMSM.

Existing offline methods to solving MTPA for the WRSM include the addition of a cross-coupled torque term and decreasing the inductance in saturation. This method produces a high order torque equation with ten terms that is challenging to optimize but nonetheless can be mapped to a dense LUT for high accuracy at the expense of high memory usage [16]. Online methods to solving MTPA with a nonlinear magnetic flux include computing the real-time parameters of the machine (resistance, inductance) using Extended Kalman Filters. Then Ferrari's method is used several times to reach a solution within some range of error [17], [18]. This method is computationally intense on a micro-controller.

This research proposes a method to create three different MTPA functions using simulated or experimental machine values: one using pareto-optimal values as points for a MTPA current path, and two using convex pareto-optimal values. In all three cases a Piecewise Affine (PWA)

B. Steyaert and M. Preindl are with the Department of Electrical Engineering, Columbia University in the City of New York, New York, NY 10027, USA (e-mail: bernard.steyaert@columbia.edu; matthias.preindl@columbia.edu).

E.B. Swint and W.W. Pennington are with Tau Motors, Inc., Redwood City, CA 94063, USA (email: ethan@taumotors.com; wesley@taumotors.com).

Color versions of one or more of the figures in this paper are available online at http://ieeexplore.ieee.org.

This article has been accepted for publication in IEEE Transactions on Transportation Electrification. This is the author's version which has not been fully edited and content may change prior to final publication. Citation information: DOI 10.1109/TTE.2023.3236526

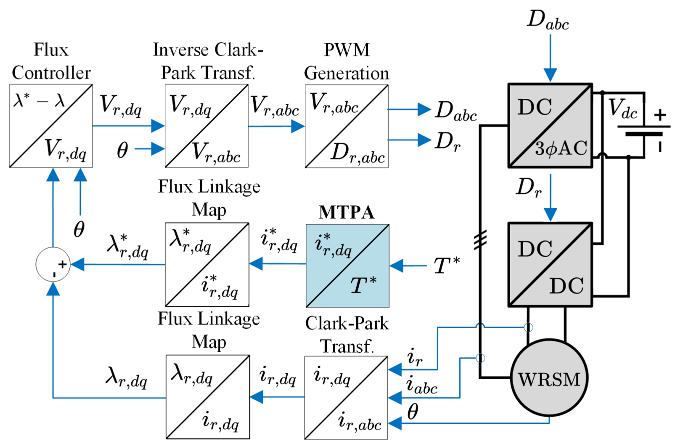

Fig. 1: WRSM motor drive (gray) with an example motor controller (white) using MTPA function (blue) to generate reference current from reference torque

MTPA function is created using the values. This produces a set of computationally inexpensive linear functions for any reference torque. Nonlinear magnetic flux (saturation and cross saturation) is included as it is present in the experimental or simulated points. The three MTPA functions are optimized for lowest copper loss, lowest torque error, and lowest computation time, respectively.

This paper is organized as follows: the WRSM dynamic model is presented in Section II. The torque and power loss characteristics for the WRSM are explained in Section III, then the MTPA optimization problem and solution sets are described in Section IV. The PWA map linking the solution sets to a continuous MTPA path in three-dimensional current space is presented in Section V. Results for an experimental setup are shown in Section VI, and finally Section VII concludes the paper.

II. WRSM Motor Model

The three-phase WRSM can be described dynamically as a state-space model [19]. For formal simplicity and the common challenges of displaying spaces higher than three, this research focuses on the most common WRSM used in motor drives: a neutral-point isolated machine (without zero-axis flux and current) and without damper windings. However, it is noted that it is trivial to generalize this research to higher dimensions. Throughout this research, we use the power-invariant Clarke transformation and the magnetic axis of the field winding is used as reference angle of the Park transformation.

The voltage equations of this WRSM are

$$\dot{\lambda}_r = v_r - R_r i_r \qquad = \bar{v}_r, \tag{1a}$$
$$\dot{\lambda}_d = \omega\lambda_q + v_d - R_s i_d \qquad = \omega\lambda_q + \bar{v}_d, \tag{1b}$$
$$\dot{\lambda}_q = -\omega\lambda_d + v_q - R_s i_q \qquad = -\omega\lambda_d + \bar{v}_q, \tag{1c}$$

where $\dot{}$ is the $\frac{d}{dt}$ operator; $\lambda_r \in \mathbb{R}$ is the rotor, i.e. field, flux linkage; $\lambda_d, \lambda_q \in \mathbb{R}$ are the d-axis and q-axis stator flux linkages respectively; $i \in \mathbb{R}$ and $v \in \mathbb{R}$ are the currents and voltages of the appropriate dimension; $R_r, R_s \in \mathbb{R}^+$ are the rotor and stator resistances, and $\omega \in \mathbb{R}$ is the synchronous speed, i.e. the electrical velocity of the machine. Furthermore, we introduce the voltages $\bar{v}$ that are the terminal voltages compensated by the winding resistive voltage drop. This concept can be generalized to include compensation for inverter nonlinear behavior such as switch on-voltage drops and dead-times [20]. The machine currents map onto machine flux with a nonlinear map $\phi : \mathbb{R}^3 \rightarrow \mathbb{R}^3$

$$\lambda_r = \phi_r(i_r, i_d, i_q), \tag{2a}$$
$$\lambda_d = \phi_d(i_r, i_d, i_q), \tag{2b}$$
$$\lambda_q = \phi_q(i_r, i_d, i_q), \tag{2c}$$

that captures magnetic coupling between axis, magnetic saturation, and cross-saturation [19]. These equations can be written as a standard state-space system in discrete time with sampling period T_s

$$\lambda^+ = f(\lambda, \bar{v}), \tag{3a}$$
$$i = g(\lambda), \tag{3b}$$

where the state is the flux $\lambda = [\lambda_r, \lambda_d, \lambda_q]^T \in \Lambda$, the input is the compensated voltage $\bar{v} = [\bar{v}_r, \bar{v}_d, \bar{v}_q]^T \in \mathcal{V}$, and the measurement is the current $i = [i_r, i_d, i_q]^T \in \mathcal{I}$. The state-space variables are finite in all dimensions and are approximated with box constraints

$$\mathcal{I} = \{i \in \mathbb{R}^3 | I_{\min} \leq i \leq I_{\max}\}, \tag{4a}$$
$$\mathcal{V} = \{\bar{v} \in \mathbb{R}^3 | \bar{V}_{\min} \leq \bar{v} \leq \bar{V}_{\max}\}. \tag{4b}$$

The flux constraint is defined as a derivative of the current constraint $\Lambda = \phi \circ \mathcal{I}$. Furthermore, the flux (and current) constraints are chosen such that the rotor flux (and current) is positive $\lambda_r \geq 0$ (and $i_r \geq 0$) without loss of generality.

The dynamic equation is expressed in vector notation as [21]

$$f(\lambda, v) = (\mathbf{I} - \omega T_s \mathbf{J})\lambda + T_s \bar{v}, \tag{5}$$

where $\mathbf{J}$ is the 90° rotation matrix in the dq plane

$$\mathbf{J} = \begin{bmatrix} 0 & 0 & 0 \\ 0 & 0 & -1 \\ 0 & 1 & 0 \end{bmatrix}. \tag{6}$$

The output function $g : \mathbb{R}^3 \rightarrow \mathbb{R}^3$ is the inverse of the nonlinear flux map $\phi(\cdot) = [\phi_r(\cdot), \phi_d(\cdot), \phi_q(\cdot)]^T$. Typically, $\phi(\cdot)$ is bijective and the output function is defined as

$$g(\lambda) = \phi^{-1}(i). \tag{7}$$

The map $\phi(\cdot)$ is typically obtained with with finite element analysis (FEA) or obtained with experimental measurement campaigns. The equation for relating current to flux linkage in the WRSM without saturation has the form

$$\lambda = \mathbf{L}i + \psi, \tag{8}$$

where $\mathbf{L} \in \mathbb{R}^+_{3\times3}$ is the inductance matrix and $\psi \in \mathbb{R}_{3\times1}$ is the flux-offset vector

$$\mathbf{L} = \begin{bmatrix} L_{rr} & L_{rd} & L_{rq} \\ L_{dr} & L_{dd} & L_{dq} \\ L_{qr} & L_{qd} & L_{qq} \end{bmatrix}, \quad \psi = \begin{bmatrix} \psi_r \\ \psi_d \\ \psi_q \end{bmatrix}. \tag{9}$$

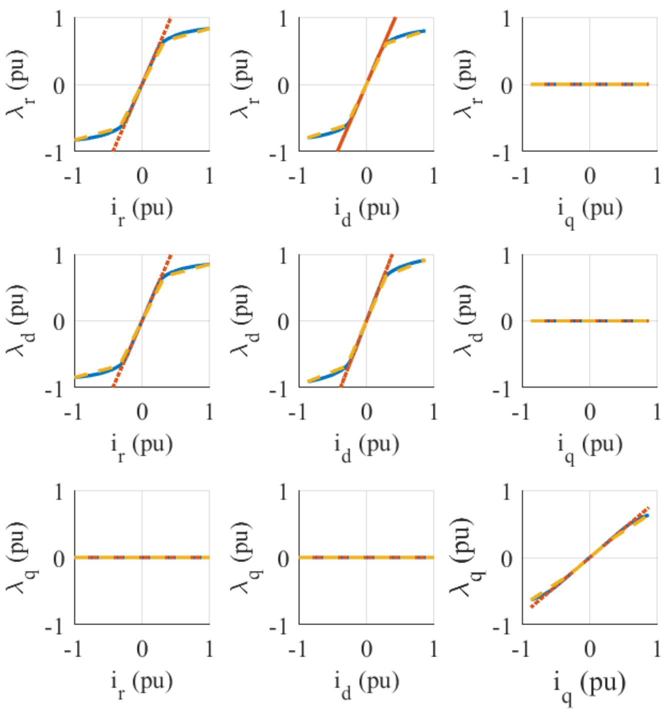

Fig. 2: WRSM flux vs current: experimental (blue), example linearization through origin (orange), example of three-segment PWA (yellow)

The diagonal terms of $\mathbf{L}$ are the self-inductances of the rotor (L_{rr}) and stator (L_{dd}, L_{qq}), while the non-diagonal terms are the mutual inductances between the three axis. Typically L_{rq}, L_{dq}, L_{qr}, and L_{qd} are negligible. In this formulation $\mathbf{L}$ is constant and the fluxes are linearized as shown in Fig. 2.

III. Motor Torque and Power Loss Models

In many machine applications, the input to the control system is a desired or reference torque T^* [Nm], while the controller is able to directly actuate winding rotor and stator voltages $\bar{v}$ and thus currents i. Thus it is desirable to create a direct mapping between torque and current in a way that minimizes electrical losses in the machine. For the WRSM an example control diagram is shown in Fig. 1.

The power invariant machine torque per pole pair is

$$\tau_p(i,\lambda) = \tau(i,\lambda)/p = i^T \mathbf{J} \lambda, \tag{10}$$

where $\tau : \mathbb{R}^6 \to \mathbb{R}$ is the machine torque and p is the number of pole pairs.

Expanding (10) using (8) yields the quadratic equation

$$\tau_p(i) \approx i^T \mathbf{J} \mathbf{L} i + i^T \mathbf{J} \psi, \tag{11}$$

a linearized approximation of $\tau_p(i)$ using $\phi(\cdot)$. $\tau_p(i) = T^*$ can be shown to be a saddle point of $\tau_p(i)$, as the Hessian matrix $\mathbf{H}(\tau_p(i) = T^*)$ has positive and negative eigenvalues.

The proposed MTPA concept can be combined with any copper loss models. The simplest has quadratic terms for

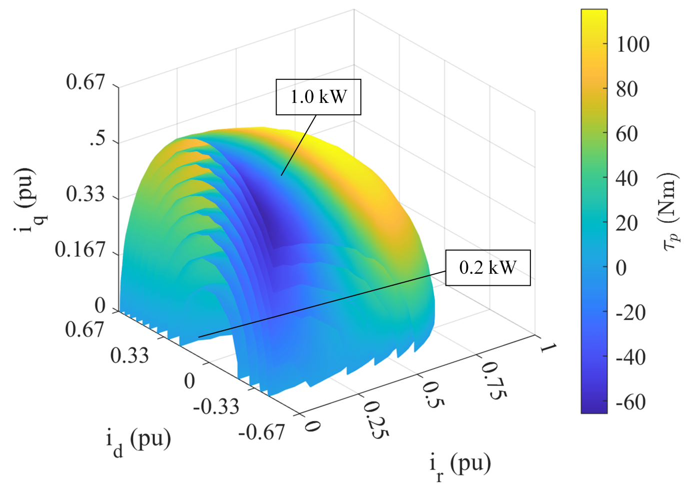

Fig. 3: $P_l = \pi_{lc}(i,\lambda)$ for $P_l = \{$0.2 kW, 0.3 kW, 0.4 kW, 0.5 kW, 0.6 kW, 0.7 kW, 0.8 kW, 0.9 kW, 1.0 kW$\}$

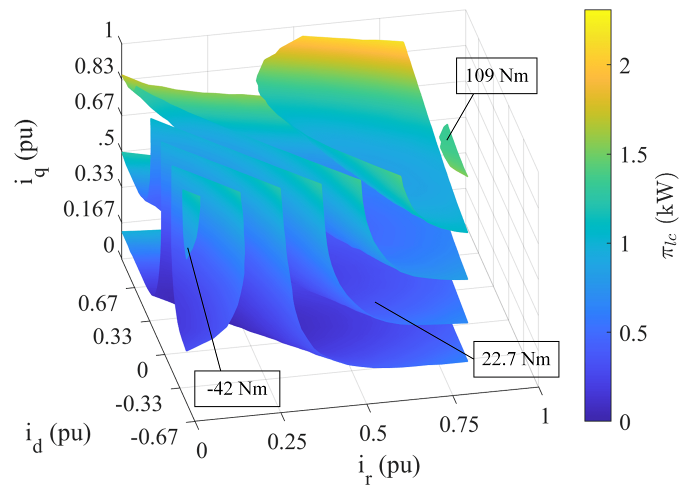

Fig. 4: $T_p = \tau_p(i,\lambda)$ for $T_p = \{-42$ Nm/p, -20.4 Nm/p, 1.1 Nm/p, 22.7 Nm/p, 44.3 Nm/p, 65.9 Nm/p, 87.4 Nm/p, 109 Nm/p$\}$

winding losses $\pi_{lc} : \mathbb{R}^6 \to \mathbb{R}$ of an electric motor [22]. In this study copper loss is approximated by $\phi(\cdot)$ and modelled as

$$\pi_{lc}(i,\lambda) \approx i^T \mathbf{R} i, \tag{12}$$

defined over the sets (19) and (18).

The matrix $\mathbf{R}$ defines the winding resistances that approximates DC and (skin effect and proximity effect) AC winding losses [23], [24]. Iso-copper-loss and iso-torque surfaces are shown in Fig. 3 and Fig. 4 respectively.

IV. Maximum Torque per Ampere

A. Problem Statement

MTPA targets minimizing copper losses (12) for a given reference torque T_p^*. The output is a reference current i^* and reference flux λ^*. The most general form of the problem is stated as follows: for a torque reference T_p^*, the MTPA current and flux references are

$$[i^*, \lambda^*] = \underset{i\in\mathcal{I},\lambda\in\Lambda,\bar{v}\in\mathcal{V}}{\arg\min} \quad \pi_{lc}(i,\lambda), \tag{13a}$$

$$\text{subj. to} \quad f(\lambda,\bar{v}) = \lambda, \tag{13b}$$

$$g(\lambda) = i, \tag{13c}$$

$$\tau_p(i,\lambda) = T_p^*. \tag{13d}$$

The objective function (13a) being minimized is electrical losses (12). Constraint (13b) is the flux λ and voltage $\bar{v}$ relationship from (1) and requires steady state operating points ($\dot{\lambda} = 0$). Constraint (13c) links current to flux using $\phi(\cdot)$, and (13d) constrains the quadratic torque function to the specific reference torque of interest T_p^*.

The solution set for all $T_p^* \in \mathcal{T}$, where $\mathcal{T}$ is the set of allowable machine torques, will be sets of currents $\underline{\mathcal{I}}$, fluxes $\underline{\Lambda}$, torques $\underline{\mathcal{T}}$, and power losses $\underline{\mathcal{P}}$ where

$$\underline{\mathcal{I}} = \{i^* \in \mathcal{I}, \text{s.t. Eqn. 13}\} \in \mathbb{R}^3 \tag{14a}$$

$$\underline{\Lambda} = \{\lambda^* \in \Lambda, \text{s.t. Eqn. 13}\} \in \mathbb{R}^3 \tag{14b}$$

$$\underline{\mathcal{T}} = \{T^* \in \mathcal{T}, \text{s.t. Eqn. 13}\} \in \mathbb{R} \tag{14c}$$

$$\underline{\mathcal{P}} = \{P_l^* \in \mathcal{P}, \text{s.t. Eqn. 13}\} \in \mathbb{R}. \tag{14d}$$

which we can combine as

$$\underline{\Gamma} = \{\underline{\mathcal{T}}, \underline{\mathcal{P}}, \underline{\mathcal{I}}, \underline{\Lambda}\} \in \mathbb{R}^8. \tag{15}$$

This optimization problem is NP-Hard to solve due to the functions $\pi_{lc}(i,\lambda)$, $\tau_p(i,\lambda)$, and state space model equations $f(\lambda, v)$ and $g(\lambda)$, thus there is no analytical solution for $\underline{\Gamma}$. An example solution for one specific $T_p \in \underline{\mathcal{T}}$ is shown in Fig. 5 showing torque and copper loss surfaces.

This formulation already accounts for saturation and cross saturation inside the machine because the datapoints Γ include i and λ togehter, therefore changes in inductance $\mathbf{L}$ throughout the machine are also modelled. Another dimension that can be added to the data set is a variable resistance matrix $\mathbf{R}$, either by experimental measurements or FEA-analysis. If the diagonal terms in the matrix $\mathbf{R}$ increase at the same rate with temperature, then by (12) the solution set $\underline{\Gamma}$ will stay unchanged, however losses will be higher.

B. Quantitative Solution to MTPA

This research focuses on solving the MTPA problem assuming low speed operation. In these conditions, the copper loss is dominant over core loss, and the machine operates below base speed $\omega \leq \omega_b$, i.e. no field weakening.

Taking a large sample of random experimental or simulated datapoints can yield an approximate solution to (13). FEA-simulated data points will have a current i and flux λ, while experimental data points will only have a known current i and an approximated flux λ using flux-linkage map approximations via ϕ (sometimes called virtual flux). These points can be directly mapped to a torque per pole pair T_p and copper loss π_{lc} by (10) and (12).

The set of all experimental datapoints is denoted

$$\Gamma = \{\mathcal{T}, \mathcal{P}, \mathcal{I}, \Lambda\} \in \mathbb{R}^8 \tag{16}$$

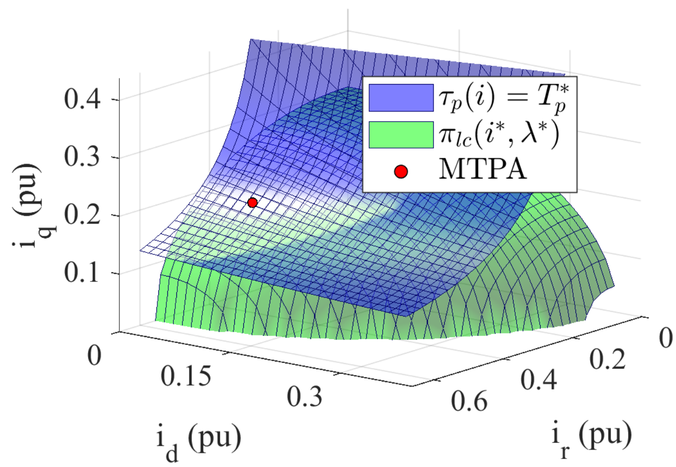

Fig. 5: Solution to MTPA showing $\tau_p(i) = T^*$ (blue), minimized $\pi_{lc}(i^*, \lambda^*)$ (green), and solution point (red).

where a single member Γ_j has four components (current, flux, torque per pole pair, power loss). The values of each component for each member can be denoted $\Gamma_{j,k}$ where j is the component and k is the index of the value. For example $\Gamma_{1,1}$ is the torque of the first data point. The set of just one component, say torque, for all points can be denoted $\Gamma_{1,k}$, while the collection of all components for one value, say the first value, can be denoted $\Gamma_{j,1}$.

The datapoints can be plotted according to their power loss, $\Gamma_{2,k}$, and inverse torque, $\Gamma_{1,k}^{-1}$ to see which points are the most optimal (minimum). From the set of all datapoints Γ, there will be pareto-optimal, or efficient, values. A pareto-optimal value is defined as a value in Γ that cannot further decrease $\Gamma_{1,k}^{-1}$ without increasing $\Gamma_{2,k}$ or vice-versa [25].

The set of all pareto-optimal points is called a pareto frontier. The pareto frontier for a WRSM can be denoted Γ_p. The points in the pareto frontier will all have unique torques. The pareto frontier points Γ_p produced by this method can be considered candidate points for a general MTPA function that will exist in three-dimensional current space $\mathcal{I}$. The curvature of the collection of lines connecting all adjacent pareto-optimal points Γ_p in the two-dimensional $\Gamma_{2,k}$ vs $\Gamma_{1,k}^{-1}$ space is not necessarily convex. A new set Γ_c is defined as the largest subset of pareto-optimal points that creates a convex function when line segments are created between the points.

The point $\Gamma_{j,x}$ that corresponds to minimum torque $T_{p,\min} \in \mathcal{T}_p$ will always be in Γ_c because the minimum torque point occurs at zero losses, and no point can have negative losses. Furthermore the point $\Gamma_{j,x}$ corresponding to maximum torque $T_{p,\max} \in \mathcal{T}_p$ will also always be in this set as no point can have higher torque, regardless of losses.

The curvature of the collection of lines connecting all adjacent Γ_c points in the three-dimensional current space ($\mathcal{I}$) is not necessarily convex. A new set Γ_{cc} is defined as the largest subset of Γ_c points that creates a convex, piecewise linear function when line segments are created between the points and grouped in the current space. The cc denotes that the piecewise linear function created is

This article has been accepted for publication in IEEE Transactions on Transportation Electrification. This is the author's version which has not been fully edited and content may change prior to final publication. Citation information: DOI 10.1109/TTE.2023.3236526

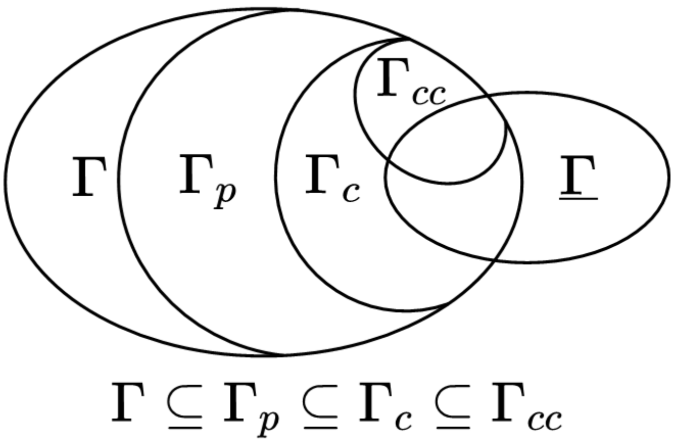

Fig. 6: Diagram showing relationship between the sets Γ, Γ_p, Γ_c, Γ_{cc}, and $\underline{\Gamma}$

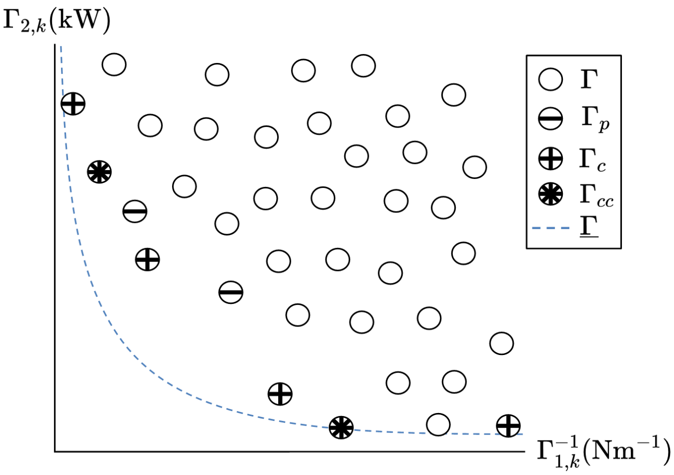

Fig. 7: Example points of $\Gamma, \Gamma_p, \Gamma_c, \Gamma_{cc}$, and $\underline{\Gamma}$ shown on power loss $\Gamma_{2,k}$ vs inverse torque $\Gamma_{1,k}^{-1}$ axis

convex in the two-dimensional ($\Gamma_{1,k}^{-1}, \Gamma_{2,k} \in \mathbb{R}^2$) space, and three-dimensional ($\Gamma_{3,k} = \mathcal{I} \in \mathbb{R}^3$) space. By these definitions $\Gamma \subseteq \Gamma_p \subseteq \Gamma_c \subseteq \Gamma_{cc}$, shown in Fig. 6.

Connecting points in Γ_c with line segments produces torque and powerloss trajectories that are more optimal than using any interior pareto-optimal points. Connecting points in Γ_{cc} with line segments produces torque and powerloss trajectories that are less optimal than using any interior pareto-optimal points. Connecting any data points using straight line segments is an approximation that is only valid for densely-sampled points. Adjacent points must be within a minimum ϵ euclidean distance of each other to be considered close enough to approximate a line between them. If two points are not close enough to meet this requirement, more points must be simulated or measured. Specifying the distance ϵ is outside the scope of this paper.

Generating a convex pareto frontier Γ_c can be obtained using a modified divide and conquer algorithm for a set of solutions [26], and repeated to obtain Γ_{cc}. Linking the line segments created using Γ_p, Γ_c, and Γ_{cc} in two-dimensional ($\Gamma_{1,k}^{-1}, \Gamma_{2,k} \in \mathbb{R}^2$) space, shown in Fig. 7, to three-dimensional ($\Gamma_{3,k} \in \mathbb{R}^3$) current space can be

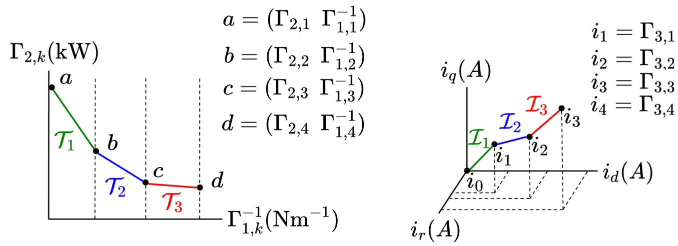

Fig. 8: (**Left**) Using four experimental data points ($\Gamma_{j,1}$, $\Gamma_{j,2}$, $\Gamma_{j,3}$, $\Gamma_{j,4}$) to partition torque-powerloss space into three one-dimensional simplices ($\mathcal{T}_1$, $\mathcal{T}_2$, $\mathcal{T}_3$); (**Right**) corresponding three, one-dimensional simplices in current space ($\mathcal{I}_1$, $\mathcal{I}_2$, $\mathcal{I}_3$)

modelled using piecewise affine maps. Each set will have unique properties.

V. Piecewise Affine Map for MTPA

This research proposes to express the approximate MTPA solution path as a piecewise-affine (PWA) function. PWA maps divide a nonlinear map into M domains over which the function is linearized [27]. The torque domain $\Gamma_{1,k}$ is partitioned into torque regions $\mathcal{T}_j$, but can equivalently be partitioned into copper loss regions. Points in this space are interchangeably described as torque per pole pair $T_{p,k}$ or $\Gamma_{1,k}$ values equivalently. The current domain $\Gamma_{3,k}$ will also be partitioned into current regions $\mathcal{I}_j$, and currents can be described by i_k or $\Gamma_{3,k}$.

Hence we express the PWA torque to current map, or MTPA function, $h(T_p)$ as

$$i = h(T_p) \approx h_{PWA}(T_p) = \begin{cases} m_1 T_p + i_1, & T_p \in \mathcal{T}_1, \\ m_2 T_p + i_2, & T_p \in \mathcal{T}_2, \\ \quad \cdots & \\ m_M T_p + i_M, & T_p \in \mathcal{T}_M, \end{cases} \tag{17}$$

where $i = m_j T_p + i_j$ is the affine equation that maps torques-powerloss points $T_p \in \mathcal{T}_j$ onto current points $i \in \mathcal{I}_j$ and $\mathcal{I}_j$ is the image of the domain $\mathcal{T}_j$. The torque simplices must cover the full range of machine torques, or $\{\mathcal{T}_1 \cup \mathcal{T}_2, \dots \mathcal{T}_M\} = \mathcal{T}$. The affine map is defined by the three-dimensional slope m_j and a current offset i_j. This is shown in Fig. 8. The points used to create $h(T)$ can be from sets Γ_p, Γ_c, or Γ_{cc}; denoted $h_p(T)$, $h_c(T)$, $h_{cc}(T)$ respectively. The process of using the points to create $h(T)$ is described next.

PWA maps divide the original domain into M sets. Each subset is defined to be a simplex, which is the simplest possible polytope in any D-dimensional space and a line segment in the single dimension of the given problem. A D-dimensional simplex can be defined as the convex hull of its $D+1$ vertices (called the V-notation; alternatively, a simplex can be defined by its by its faces defined as affine inequalities called the H-notation [28])

$$\mathcal{T}_j = \mathcal{H}(\{T_{j_0}, T_{j_1}\}), \tag{18}$$

This article has been accepted for publication in IEEE Transactions on Transportation Electrification. This is the author's version which has not been fully edited and content may change prior to final publication. Citation information: DOI 10.1109/TTE.2023.3236526

where $T_{j_0}, T_{j_1} \in \mathcal{T}$. All torques in this section are per pole pair, thus the subscript p in T_p is dropped for simplicity. Each torque simplex $\mathcal{T}_j$ forms a domain of an affine map that maps into the current simplex

$$\mathcal{I}_j = \mathcal{H}(\{i_{j_0}, i_{j_1}\}), \tag{19}$$

where $i_{j_0}, i_{j_1} \in \mathcal{I}$. The torque and current points must be from the same experimental point, i.e. T_{j_0} and i_{j_0} belong to Γ_{j,j_0}. Example simplices that are linked in both spaces are shown in Fig. 8. Each line segment $\mathcal{T}_j$ is defined by two vertices. Let one vertex T_{j_0} be the support vector such that we can move the origin $\bar{T} = T - T_{j_0}$. In the shifted dimension, the simplex is defined by

$$\bar{\mathcal{T}}_j = \mathcal{H}(\{0, \bar{T}_{j_1}\}), \tag{20}$$

where $\bar{T}_{j_1} = T_{j_1} - T_{j_0}$ and $\bar{T}_{j_1}$ spans the simplex. Furthermore, we shift the current space in the same way, $\bar{i} = i - i_{j_0}$ that results in the simplex

$$\bar{\mathcal{I}}_j = \mathcal{H}(\{0, \bar{i}_{j_1}\}), \tag{21}$$

where $\bar{i}_{j_1} = i_{j_1} - i_{j_0}$ and $\bar{i}_{j_1}$ spans the simplex. The $D = 1$ simplices and the shift of origin are illustrated in Fig. 9.

The nonzero vertices can be interpreted as a basis and since an affine map is an isomorphism, the relative position of a vector in the current and flux simplex is the same

$$\bar{T} = a\bar{T}_{j_1}. \tag{22}$$

The a coefficient can be obtained similar to how space vector modulation (SVM) computes relative on-times [27].

We project $\bar{T}$ onto the basis of $\bar{\mathcal{T}}_j$

$$p_j = \mathrm{proj}_{\bar{T}_{j_1}} \bar{T} = \frac{\bar{T}_{j_1} \cdot \bar{T}}{\|\bar{T}_{j_1}\|}, \tag{23}$$

and obtain the relative length of the vector by dividing the magnitude of the projection with the magnitude of the basis vector

$$a = \frac{\|p_j\|}{\|\bar{T}_{j_1}\|}. \tag{24}$$

To find the current vector $\bar{i}$, we multiply a with the basis vector of $\bar{i}_j$, $\bar{i}_{j_1}$

$$\bar{i} = a\bar{i}_{j_1}. \tag{25}$$

Setting the a coefficients in (22) and (25) equal

$$\frac{\bar{T}}{\bar{T}_{j_1}} = \frac{\bar{i}}{\bar{i}_{j_1}} \tag{26a}$$

and solving for i yields the resulting linear map

$$i = m_j T_p + i_j \tag{26b}$$

where $m_j = \frac{i - i_{j_0}}{T_{j_1} - T_{j_0}}$ and $i_j = i_{j_0} - m_j T_{j_0}$ A visualization of this is shown in Fig. 9.

VI. Simulated and Experimental Results

A 65 kW WRSM with the parameters listed in TABLE II is used to validate the MTPA formulation and solutions.

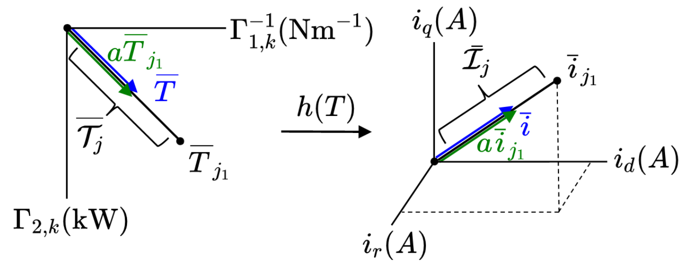

Fig. 9: (**Left**) Torque-powerloss shifted simplex $\overline{\mathcal{T}}_j$ and projected vector $\overline{T}_{j_1}$ mapped to (**right**) shifted current simplex $\bar{\mathcal{I}}_j$ and projected vector $\bar{i}$ by PWA function $h(T)$

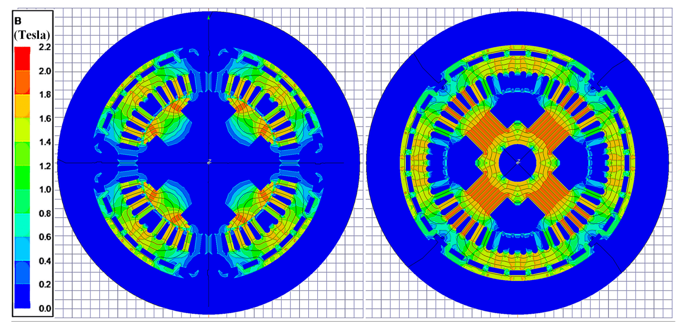

Fig. 10: WRSM cross section showing a saturated flux density B distribution in Tesla at $i_q = 1$(pu) (**left**), and $i_d = 1$(pu) (**right**)

A. Simulated Results

The WRSM was modelled computationally using the Finite Element Method (FEM) and analyzed using Finite Element Analysis (FEA). FEA approximates flux λ in the machine based on current i, machine geometry (armature windings, slip rings, saliency), and magnetic materials (core laminations), as well as parasitics (fringing, core loss, copper loss). Torque is calculated using (10). The data points obtained are evaluated over small areas using approximations to obtain an accurate model of how the machine will function full-scale. Fig. 10 shows a cross section of the machine in simulation showing the stator at fully saturated stator current (i_d and i_q) and the resulting magnetic fields. The data obtained is the full set of datapoints Γ.

The sets Γ_p, Γ_c, Γ_c are obtained in post processing by the methods described in Section IV. These sets are shown in Fig. 11 in the two-dimensional $(\Gamma^{-1}_{1,k}, \Gamma_{2,k})$ space and three-dimensional $(\Gamma_{3,k})$ space. The majority of the points from the FEA analysis are not in these sets. Of the $57,288$ generated datapoints the sizes of the sets were $|\Gamma_p| = 403$, $|\Gamma_c| = 60$, $|\Gamma_{cc}| = 47$, or less than 1%.

The MTPA functions produced using Γ_p, Γ_c, Γ_c are evaluated against a 'linear' MTPA ($h_{\mathrm{lin}}(T_p)$) which is a linear trajectory between the maximum torque point and the origin (in the current domain), as well as against a cubic spline interpolated MTPA ($h_{\mathrm{spl}}(T_p)$) which uses the points in Γ_{cc} but they are cubic spline interpolated instead of piecewise affine interpolated.

This article has been accepted for publication in IEEE Transactions on Transportation Electrification. This is the author's version which has not been fully edited and content may change prior to final publication. Citation information: DOI 10.1109/TTE.2023.3236526

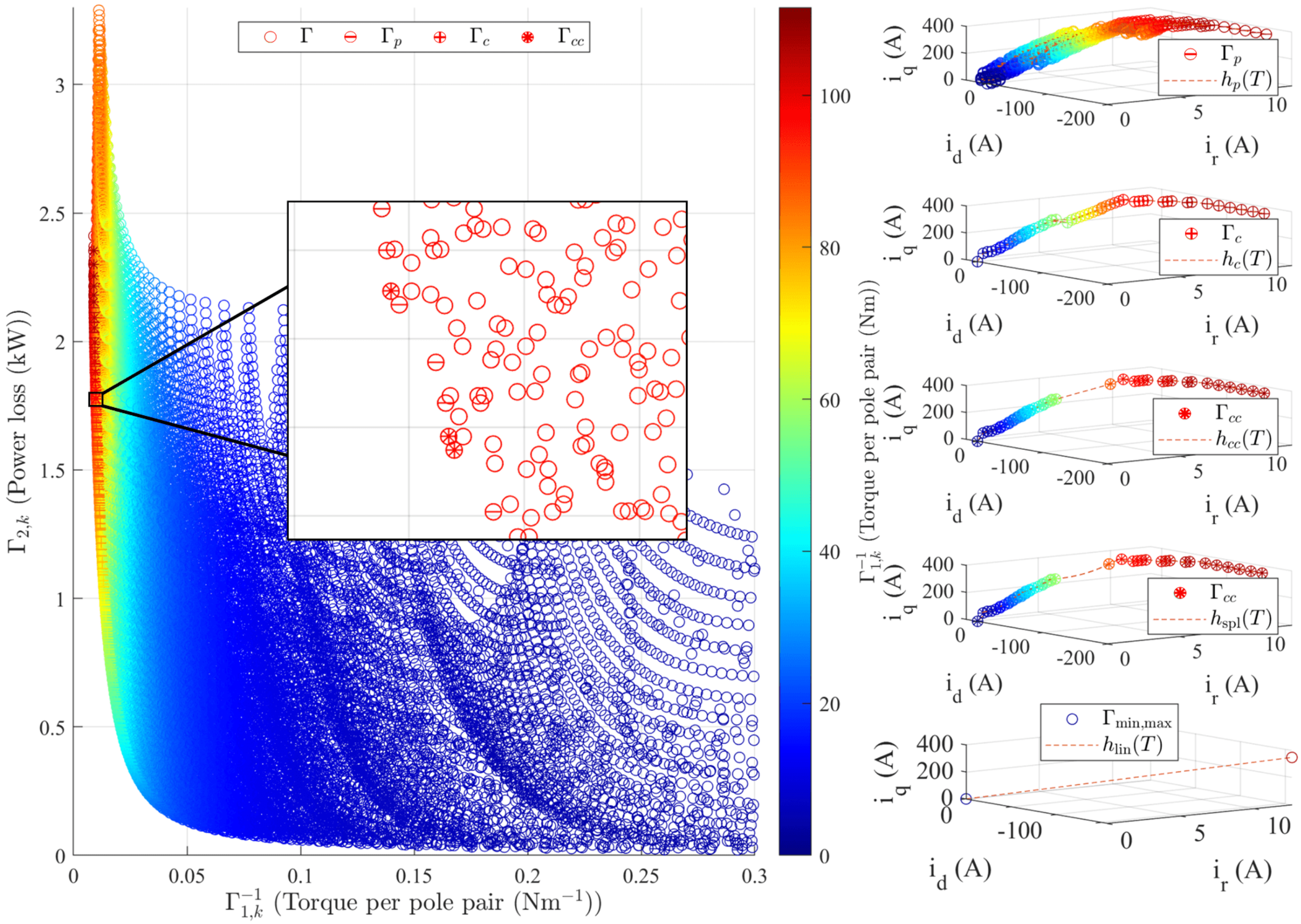

Fig. 11: FEA-Simulation results: (**Left**) Powerloss vs torque domain FEA-simulated points Γ and subsets Γ_p, Γ_c, Γ_{cc}, (**Right**) Current domain sets Γ, Γ_p, Γ_c, Γ_{cc} and functions $h_p(T_p)$, $h_c(T_p)$, $h_{cc}(T_p)$,$h_{\mathrm{spl}}(T_p)$, $h_{\mathrm{lin}}(T_p)$

B. Experimental Results

The motor testbench is shown in Fig. 12 and is configured to run using the control diagram in Fig. 1. The five $h(T_p)$ functions were translated to controller code and evaluated on a Texas Instruments TMS320F28379D real-time microcontroller to test their computation time and memory size.

In the PWA formulation, if N points are used to create each $h(T_p)$ function then $N-1$ lines (or sub-domains) are needed, therefore the memory size will grow at a rate of $\mathcal{O}(N)$ (coefficients plus boundary conditions). The cubic spline interpolation requires twice as much memory as it must save four coefficients (third degree polynomials) instead of two. The computation time of the PWA $h(T_p)$ functions has two components, a (cold start) search which takes $Nlog(N)$ time, and two floating point operations. The cubic spline $h_{\mathrm{spl}}(T_p)$ will use the same search, but requires six floating point operations via Horner's method, therefore taking three times as long; both are $\mathcal{O}(Nlog(N))$ computation time. As more inputs and outputs are added cubic spline interpolations tend to increase in complexity by factors of two over PWA [29]. $h_{\mathrm{lin}}(T_p)$ has $\mathcal{O}(1)$ computation and memory size, but is extremely inaccurate. A summary of MCU performance is shown in TABLE III. The time of the other control operations of the control loop are shown in TABLE I.

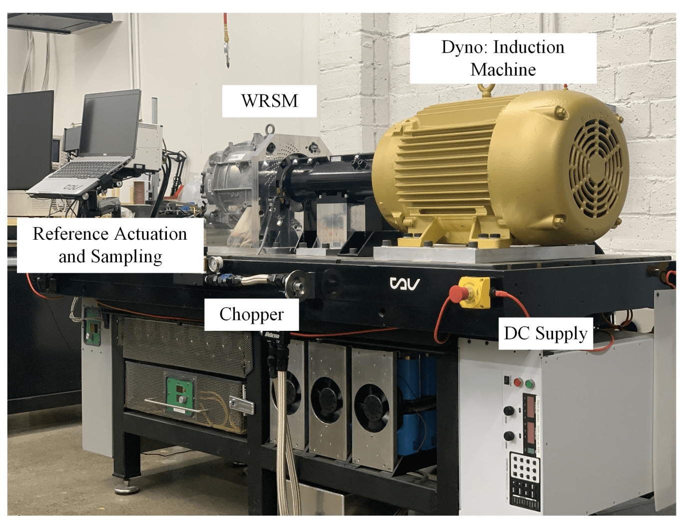

Fig. 12: WRSM bench setup: (clockwise from left) Reference Actuation and Sampling, WRSM, Dyno: Induction Machine, DC Supply, Chopper

For real-time evaluation, several tests were conducted.

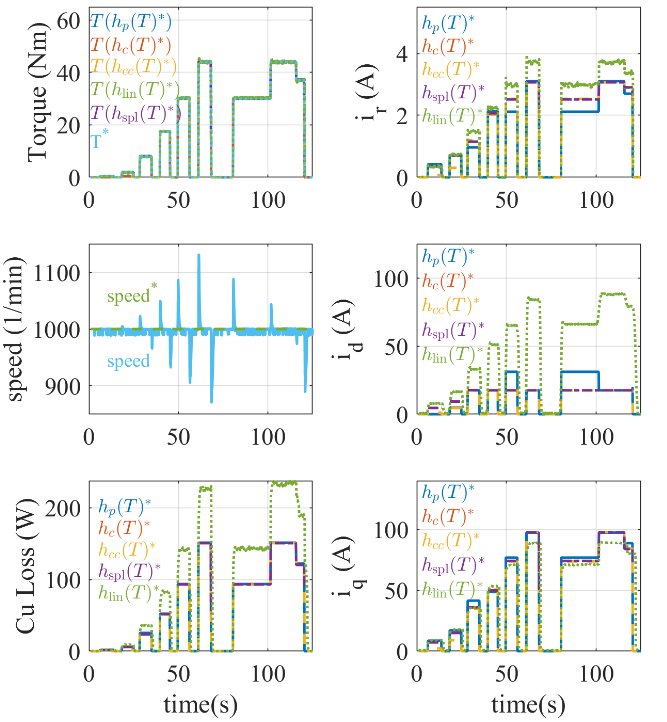

Fig. 13: 120s Experimental MTPA PWA results **(Left)** Top to bottom: Torque (reference, measured, MTPA PWA); Speed (reference and measured); Copper losses (experimental, MTPA PWA) **(Right)** Top to bottom: rotor current (measured, MTPA PWA); d-axis stator current (measured, MTPA PWA); q-axis stator current (measured, MTPA PWA)

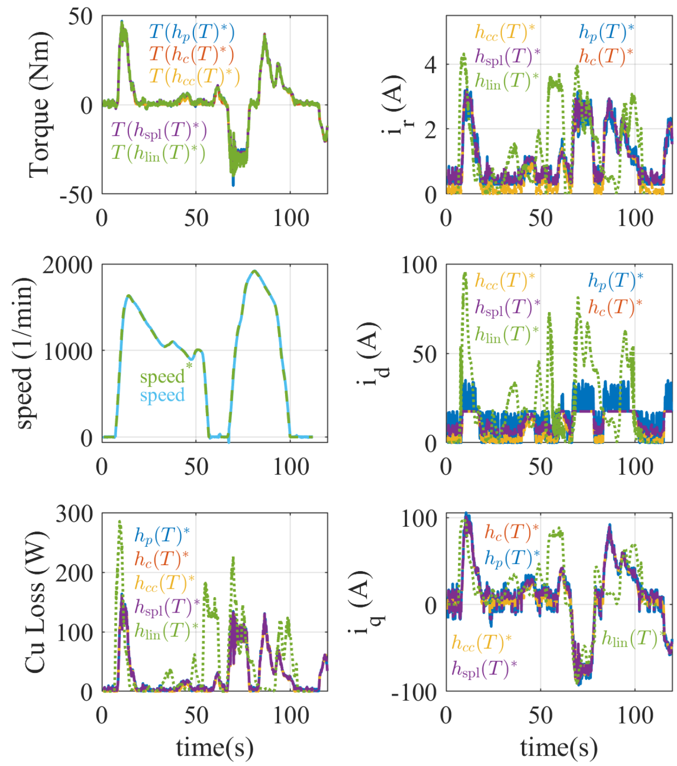

Fig. 14: Drive cycle with WRSM following dynamic speed reference (**right column top to bottom**): experimental and post-processed rotor current i_r (**top**), stator currents i_d (**middle**) and i_q (**bottom**) using the MTPA maps $h_p(T)$, $h_c(T)$, $h_{cc}(T)$, and $h_{\text{spl}}(T)$; (**left column top to bottom**) experimental torque tracking a (**middle**) speed reference, (**bottom**) real-time copper losses for each MTPA function

TABLE I: Control Timing Parameters

Operation	time (μs)
ADC Conversions	1.8
MTPA PWA Map $h_{\text{lin}}(t)$	6.0
Clarke Park Transform	6.3
Flux Linkage Maps ($\times 2$)	14.6
PI Virtual Flux Controller	6.1
Inverse Clark Park Transform	6.3
PWM Generation	3.1

The first involved the WRSM being spun at a fixed speed of 1000 1/min using a coupled industrial drive. The WRSM exerts .5 - 44 Nm variable torque steps that follow torque references over a 120s period. The experimental MTPA function used was h_{lin}. The MTPA references generated offline by $h_p(T_p)$, $h_c(T_p)$, and $h_{cc}(T_p)$ (as well as $h_{\text{spl}}(T_p)$) are shown in Fig. 13 and are applied to the requested torques in post processing. A drive cycle emulating the operation of a passenger vehicle was also conducted, where a reference speed trajectory is applied, and the coupled industrial drive simulates the nonlinear torque load due to vehicle dynamics. This experiment is useful to show the operation of the MTPA functions under dynamically changing speeds and torques (including negative torque operation). It is shown in Fig. 14. Torque is symmetrical about i_q by (11), therefore the maps $h_p(T_p)$, $h_c(T_p)$, $h_{cc}(T_p)$, and $h_{\text{spl}}(T_p)$ can handle negative torques by inputting the negative of the requested torque, $-T_p$, and then replacing i_q with $-i_q$ at the output of the function. Lastly, a close up of a torque step showing the transient behavior of the controller and MTPA functions is shown in Fig. 15.

In every experiment, the linear MTPA function $h_{\text{lin}}(T_p)$ performs the worst, creating up to 70% additional copper losses in some cases. This comes at the expense of extremely fast computation and very low memory size.

The functions $h_p(T_p)$, $h_p(T_p)$, and $h_{cc}(T_p)$ have different properties that are useful for different applications. Averaged copper loss is shown in TABLE IV, as expected from Section IV $h_c(T_p)$ outperforms $h_p(T_p)$ and $h_{cc}(T_p)$, although all three are within 1% of each other. The PWA MTPA functions outperform the cubic spline $h_{\text{spl}}(T_p)$, with the trade-off of losing smoothness in $\mathcal{I}$.

Because all of the $h(T_p)$ functions are piecewise-linear approximations of Γ, there will be error in the currents produced. This error can be quantified by comparing torque T_p (expected torque) to the resulting torque from $\tau_p(h(T_p))$, where $i = h(T_p)$ is the set of current references. This error is shown in Fig. 16. $h_c(T_p)$ and $h_{cc}(T_p)$ have minimal error at $T_p > 10$ Nm/p, and $h_p(T_p)$ has very low error throughout all torques. The spline MTPA $h_{\text{spl}}(T_p)$ and linear MTPA $h_{\text{lin}}(T_p)$ bound the PWA interpolations

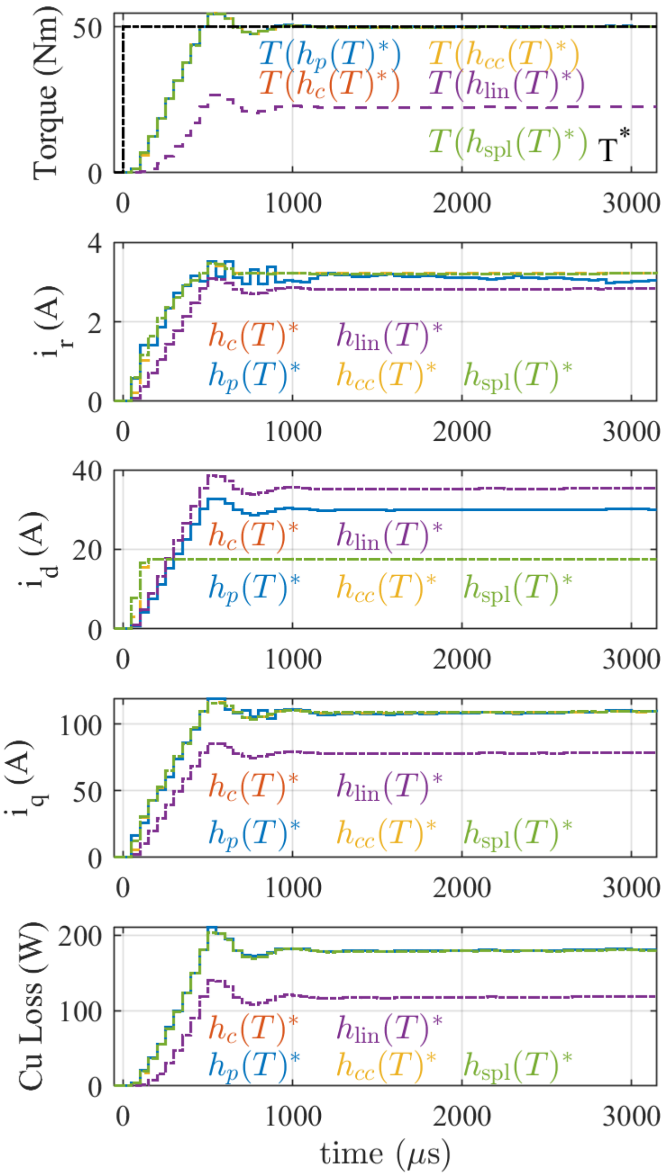

Fig. 15: 50 Nm dynamic torque step (**Top to bottom**) torque reference T^* and recalculated torques from currents $h_p(T)$, $h_c(T)$, $h_{cc}(T)$, $h_{\text{spl}}(T)$, experimental and post-processed rotor current i_r and stator currents i_d, i_q generated from $h_p(T)$, $h_c(T)$, $h_{cc}(T)$, $h_{\text{spl}}(T)$ MTPA functions, real-time copper losses for each MTPA function

in torque error. This error presents itself in each of the torque plots of Fig. 13, Fig. 14, Fig. 15 as well.

Finally, the shape of the MTPA trajectory for each $h(T_p)$ is different. $h_p(T_p)$ is very jagged, and even a small torque change produces large differences in current (as seen in Fig. 13). $h_{cc}(T_p)$ is the least jagged, and has the property of being convex in $\mathcal{I}$. $h_c(T_p)$ is a compromise between the two.

In summary the PWA MTPA functions are reasonable in terms of memory, computation time, average copper loss, and torque error, however some perform very well in some categories:

- $h_p(T_p)$: low torque error
- $h_c(T_p)$: low average copper loss
- $h_{cc}(T_p)$: fast computation time, small memory, convex

The two reference MTPA functions tend to operate on extremes of two or more criteria

- $h_{\text{lin}}(T_p)$: fast computation, small memory, very high error, very high average copper loss
- $h_{\text{spl}}(T_p)$: low torque error, slow computation time

TABLE II: WRSM Motor Drive Parameters

Parameter	**Value**
Turns ratio N_f/N_s	39
Pole pairs p	2
Stator resistance R_s	11.732 mΩ
Rotor resistance (stator referred) R_r	5.461 mΩ
Shaft inertia	22.76E-3 kg m^2
Switching frequency	10 kHz
Sampling frequency	20 kHz
Nameplate r-axis inductance L_r	1.956 mH
Nameplate d-axis inductance L_d	2.420 mH
Nameplate q-axis inductance L_q	0.789 mH
Base speed	3000 1/min
DC-link voltage	325 V
Maximum power	65 kW
Maximum torque	220 Nm

TABLE III: MCU Performance of MTPA Functions

	Comp. Time (μs)	**Memory (KiB)**
$h_{\textbf{lin}}(T)$	6	4
$h_p(T)$	226	102
$h_c(T)$	40	18
$h_{cc}(T)$	**24**	**15**
$h_{\textbf{spl}}(T)$	72	31

TABLE IV: Efficiency and Accuracy of MTPA Functions

	Avg. π_{lc} (W)	**Avg. T error (%)**	**Convex in $\mathcal{I}$**
$h_{\textbf{lin}}(T)$	950	29.9	yes
$h_p(T)$	761.7	**0.16**	no
$h_c(T)$	**758.9**	1.68	no
$h_{cc}(T)$	759.0	1.69	**yes**
$h_{\textbf{spl}}(T)$	761.9	.07	yes

VII. Conclusion

In this study, the Maximum Torque per Ampere (MTPA) problem was presented for the WRSM, and three numerical solutions were proposed each with differing pros and cons. The solution sets were chosen using pareto optimal and convex points, which were linked together in three-dimensional current space using Piecewise Affine (PWA) functions to create a continuous current path for all machine torques. The solutions were each validated and compared using an experimental bench setup and show reduction of torque error by $> 25\%$, reduction of average copper loss by $> 20\%$ compared to a conventional linear MTPA map, and had reasonable computation time and memory usage. The functions were created using FEA-simulated points and experimentally tested on a 65 kW test setup.

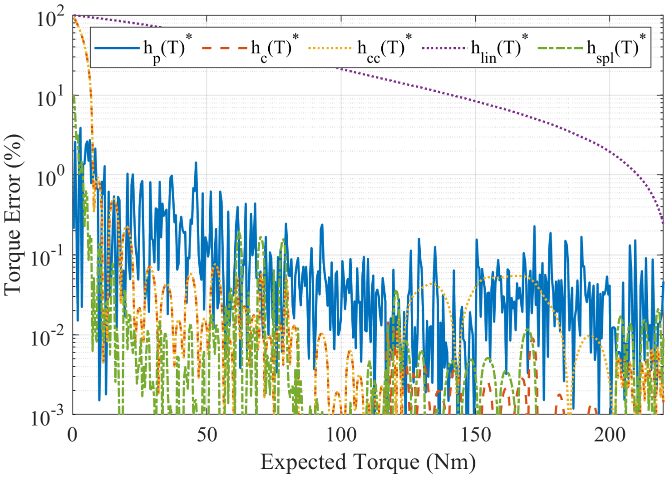

Fig. 16: Torque error vs expected torque for five MTPA functions $h_p(T)$, $h_c(T)$, $h_{cc}(T)$, $h_{\mathrm{lin}}(T)$, $h_{\mathrm{spl}}(T)$

References

[1] B. Steyaert, E. Swint, W. W. Pennington, and M. Preindl, "Piecewise affine maximum torque per ampere for the wound rotor synchronous machine," in *2022 IEEE Transp. Electr. Conf. and Expo (ITEC)*, pp. 356–363, 2022.

[2] J. de Santiago, H. Bernhoff, B. Ekergard, S. Eriksson, S. Ferhatovic, R. Waters, and M. Leijon, "Electrical Motor Drivelines in Commercial All-Electric Vehicles: A Review," *IEEE Trans. Veh. Technol.*, vol. 61, no. 2, pp. 475–484, Feb. 2012.

[3] C. Rossi, D. Casadei, A. Pilati, and M. Marano, "Wound Rotor Salient Pole Synchronous Machine Drive for Electric Traction," in *Conf. Rec. IEEE Ind. Appl. Conf., IAS Annu. Meet.*, vol. 3, pp. 1235–1241, Oct. 2006, iSSN: 0197-2618.

[4] A. Doria-Cerezo, V. I. Utkin, R. S. Munoz-Aguilar, and E. Fossas, "Control of a Stand-Alone Wound Rotor Synchronous Generator: Two Sliding Mode Approaches via Regulation of the d-Voltage Component," *IEEE Trans. Control Syst. Technol.*, vol. 20, no. 3, pp. 779–786, May. 2012.

[5] A. Dòria-Cerezo, C. Batlle, and G. Espinosa-Pérez, "Passivity-based control of a wound-rotor synchronous motor," *IET Control Theory & Appl.*, vol. 4, pp. 2049–2057, 2010.

[6] Y. Miao, H. Ge, M. Preindl, J. Ye, B. Cheng, and A. Emadi, "Mtpa fitting and torque estimation technique based on a new flux-linkage model for interior-permanent-magnet synchronous machines," *IEEE Trans. on Ind. Appl.*, vol. 53, no. 6, pp. 5451–5460, 2017.

[7] N. Bedetti, S. Calligaro, and R. Petrella, "Stand-Still Self-Identification of Flux Characteristics for Synchronous Reluctance Machines Using Novel Saturation Approximating Function and Multiple Linear Regression," *IEEE Trans. Ind. Appl.*, vol. 52, no. 4, pp. 3083–3092, Jul. 2016.

[8] H. Chen, C. Sun, and Q. Wang, "Analysis of Flux-Linkage Characteristics of Switched Reluctance Linear Generator," *IEEE Trans. Appl. Supercond.*, vol. 24, no. 3, pp. 1–5, Jun. 2014.

[9] H. Chen, W. Yan, and Q. Wang, "Electromagnetic Analysis of Flux Characteristics of Double-Sided Switched Reluctance Linear Machine," *IEEE Trans. Appl. Supercond.*, vol. 26, no. 4, pp. 1–7, Jun. 2016.

[10] A. Di Gioia, I. P. Brown, Y. Nie, R. Knippel, D. C. Ludois, J. Dai, S. Hagen, and C. Alteheld, "Design and Demonstration of a Wound Field Synchronous Machine for Electric Vehicle Traction With Brushless Capacitive Field Excitation," *IEEE Trans. Ind. Appl.*, vol. 54, no. 2, pp. 1390–1403, Mar. 2018.

[11] P. Haghgooei, B. Nahid-Mobarakeh, N. Takorabet, and D. Arab-Khaburi, "Online Stator Flux Estimation for a Wound Rotor Synchronous Machine (WRSM)," in *Ind. Appl. Soc. IEEE-IAS Annu. Meet.*, pp. 1–6, Oct. 2020, iSSN: 2576-702X.

[12] P. Haghgooei, E. Jamshidpour, N. Takorabet, D. Arab-khaburi, and B. Nahid-Mobarakeh, "Magnetic Model Identification of Wound Rotor Synchronous Machine Using a Novel Flux Estimator," *IEEE Trans. on Ind. Appl.*, pp. 1–1, 2021.

[13] K. Liu, J. Feng, S. Guo, L. Xiao, and Z.-Q. Zhu, "Identification of Flux Linkage Map of Permanent Magnet Synchronous Machines Under Uncertain Circuit Resistance and Inverter Nonlinearity," *IEEE Trans. Industr. Inform.*, vol. 14, no. 2, pp. 556–568, Feb. 2018.

[14] Y. Nie, D. C. Ludois, and I. P. Brown, "Deadbeat-Direct Torque and Flux Control of Wound Field Synchronous Machine at Low Sampling to Fundamental Frequency Ratios," *IEEE Trans. Ind. Appl.*, vol. 55, no. 4, pp. 3813–3822, Jul. 2019.

[15] M. Seilmeier and B. Piepenbreier, "Identification of steady-state inductances of PMSM using polynomial representations of the flux surfaces," in *IECON - 39th Annu. Conf. IEEE Ind. Electron. Soc.*, pp. 2899–2904, Nov. 2013, iSSN: 1553-572X.

[16] J. Pang, W. Liu, N. Jiao, J. Wang, and P. Ma, "Calculation of Cross-Coupling Inductance and Electromagnetic Torque in Wound-Rotor Synchronous Starter/Generator," *IEEE Trans. Ind. Electron*, vol. 66, no. 7, pp. 5115–5123, Jul. 2019.

[17] Y. Zhang, W. Liu, Q. jia, N. Jiao, and J. Pang, "Maximum Torque per Ampere Control with Inductance and Field Current Estimation for Wound-Rotor Synchronous Starter/Generator," in *23rd Int. Conf. Electr. Mach. Syst. (ICEMS)*, pp. 172–176, Nov. 2020.

[18] Y. Kim and K. Nam, "Copper-Loss-Minimizing Field Current Control Scheme for Wound Synchronous Machines," *IEEE Trans. Power Electron*, vol. 32, no. 2, pp. 1335–1345, Feb. 2017.

[19] I. Canay, "Causes of discrepancies on calculation of rotor quantities and exact equivalent diagrams of the synchronous machine," vol. PAS-88, pp. 1114–1120.

[20] M. Preindl and S. Bolognani, "Optimal state reference computation with constrained mtpa criterion for pm motor drives," *IEEE Trans. Power Electron.*, vol. 30, no. 8, pp. 4524–4535, 2015.

[21] M. Preindl, "Robust control invariant sets and lyapunov-based mpc for ipm synchronous motor drives," *IEEE Trans. on Ind. Elect.*, vol. 63, no. 6, pp. 3925–3933, 2016.

[22] S. D. Sudhoff, *Transformer Design*, pp. 205–253, 2014.

[23] N. Kutkut, D. Novotny, D. Divan, and E. Yeow, "Analysis of winding losses in high frequency foil wound inductors," in *1995 IEEE Ind. Appl. Conf. 30th Annual Meeting*, vol. 1, pp. 859–867 vol.1, 1995.

[24] M. Eull, L. Zhou, M. Jahnes, and M. Preindl, "Bidirectional nonisolated fast charger integrated in the electric vehicle traction drivetrain," *IEEE Trans. on Transp. Elect.*, vol. 8, no. 1, pp. 180–195, 2022.

[25] V. Pareto, *Manual of political economy (manuale di economia politica)*. New York: Kelley, 1971 (1906), translated by Ann S. Schwier and Alfred N. Page.

[26] L. He, A. Friedman, and C. Bailey-Kellogg, "A divide-and-conquer approach to determine the pareto frontier for optimization of protein engineering experiments," *Proteins*, vol. 80, pp. 790–806, 03 2012.

[27] P. Samuel and S. Levy, *Projective Geometry*, ser. Undergraduate Texts in Mathematics. Springer New York, 1988.

[28] F. Borrelli, A. Bemporad, and M. Morari, "Predictive control for linear and hybrid systems," 2017.

[29] T. H. Cormen, C. E. Leiserson, R. L. Rivest, and C. Stein, *Introduction to Algorithms*, 2nd ed. The MIT Press, 2001.

Bernard Steyaert (S'21) received a B.A. in Pre-Engineering Ursinus College (*summa cum laude, salutatorian*), B.Sc. and M.Sc. in Electrical Engineering from Columbia University in 2019, 2020, and 2022 respectively. He is currently pursuing a Ph.D. in Electrical Engineering with the Motor Drives and Power Electronics Laboratory at Columbia University. Research interests include control optimization for motor drives, as well as grid technologies.

Ethan Swint (M'04) received B.Sc. in electrical and computer engineering from Baylor University (2002), M.Sc. in mechanical engineering from University of Texas-Austin (2004), and Ph.D in electrical engineering from Virginia Tech (2012). He has been involved in the design and implementation of motor drive systems in companies ranging from startup to blue-chip, prototype to high-volume production. Since his doctoral work on switched reluctance machines, his interests have been on the integrated design of motor drive components - machines, electronics, and controls. Previously, he worked on design and manufacturing of a high-efficiency linear machine at Mainspring Energy, lead the third-generation motor designs from concept to production at Tesla, and fast-turn design-to-production of PM machines for a variety of applications with diameters ranging from 7mm-450mm at Celeramotion. Presently, he works to lead the development of motor drive systems which improve power density, efficiency, durability, economics, and sustainability at Tau Motors.

W. Wesley Pennington (M'21) is an entrepreneur and scientist focused on the research, development, and progress of emerging, deep technology across transformational industries. Presently, he is the Founder and CEO of Tau Motors, Inc. where he leads the company to build advanced technologies for electrification and energy systems to enable the transition to a more sustainable future. Wesley has a background as a technologist across a number of disciplines from applied AI to bioengineering. Previously, he was appointed to the faculty of management at the Kelley School of Business and worked in early-stage venture to develop and commercialize innovations out of academic and laboratory settings. He received a B.Sc. in biodynamics, Cert. management and human organization (*cum laude*), M.Sc. in human factors and biomechanics, and is a Ph.D candidate in cognitive neuromotor control all at Indiana University, where he is currently on leave as he builds Tau.

Matthias Preindl (S'12-M'15-SM'18) received the B.Sc. degree in electrical engineering (*summa cum laude*) from the University of Padua, Italy, the M.Sc. degree in electrical engineering and information technology from ETH Zurich, Switzerland, and the Ph.D. degree in energy engineering from the University of Padua, in 2008, 2010, and 2014, respectively. He is currently Associate Professor of Power Electronic Systems in the Department of Electrical Engineering at Columbia University, USA. Prior to joining Columbia University in 2016, he was an R&D Engineer of Power Electronics and Drives at Leitwind AG, Italy (2010-2012), a Post Doctoral Research Associate with the McMaster Institute for Automotive Research and Technology, McMaster University, Hamilton, ON, Canada (2014-2015), and a Sessional Professor in the Department of Electrical and Computer Engineering, McMaster University (2015). He serves as the area editor of vehicular electronics and systems at the IEEE Transactions on Vehicular Technology and as the general chair of the 2022 IEEE/AIAA ITEC+EATS. He received several awards and honors including the Horiba Awards Honorable Mention (Japan, 2019), the Futura Foundation Award (Italy, 2017), the NSF CAREER Award (USA, 2017), and he is the co-recipient of several best paper and presentation recognitions including the 2019 IEEE Transactions on Industrial Electronics best paper award.